

Temperature and emissivity separation from ASTER data for low spectral contrast surfaces

César Coll, Vicente Caselles, Enric Valor, Raquel Niclòs, Juan M. Sánchez, Joan M. Galve and Maria Mira
Department of Earth Physics and Thermodynamics, Faculty of Physics, University of Valencia.
50, Dr. Moliner. 46100 Burjassot, SPAIN. Email: cesar.coll@uv.es

ABSTRACT

The performance of Advanced Spaceborne Thermal Emission Reflection Radiometer (ASTER) thermal infrared (TIR) data product algorithms was evaluated for low spectral contrast surfaces (such as vegetation and water) in a test site close to Valencia, Spain. Concurrent ground measurements of surface temperature, emissivity, and atmospheric radiosonde profiles were collected at the test site, which is a thermally homogeneous area of rice crops with nearly full vegetation cover in summer. Using the ground data and the local radiosonde profiles, at-sensor radiances were simulated for the ASTER TIR channels and compared with LIB data (calibrated at-sensor radiances) showing discrepancies up to 3 % in radiance for channel 10 at 8.3 μm (equivalently, 2.5 $^{\circ}\text{C}$ in temperature or 7 % in emissivity), whereas channel 13 (10.7 μm) yielded a closer agreement (maximum difference of 0.5 % in radiance or 0.4 $^{\circ}\text{C}$ in temperature). We also tested the ASTER standard products of land surface temperature (LST) and spectral emissivity generated with the Temperature-Emissivity Separation (TES) algorithm with standard atmospheric correction from both global data assimilation system profiles and climatology profiles. These products showed anomalous emissivity spectra with lower emissivity values and larger spectral contrast (or maximum-minimum emissivity difference, MMD) than expected, and as a result, overestimated LSTs. In this work, a scene-based procedure is proposed to obtain more accurate MMD estimates for low-spectral contrast materials (vegetation and water) and therefore a better retrieval of LST and emissivity with the TES algorithm. The method uses various gray-bodies or near gray-bodies with known emissivities and assumes that the calibration and atmospheric correction performed with local radiosonde data are accurate for channel 13. Taking the channel 13 temperature (atmospherically and emissivity corrected) as the true LST, the radiances for the other channels were simulated and used to derive linear relationships between ASTER digital numbers and at-ground radiances for each channel. The TES algorithm was applied to the adjusted radiances and the resulting products showed a closer agreement with the ground measurements (differences lower than 1 % in channel 13 emissivities and within ± 0.3 $^{\circ}\text{C}$ in temperature for rice and sea pixels).

1. INTRODUCTION

The Advanced Spaceborne Thermal Emission Reflection Radiometer (ASTER) is a high spatial resolution radiometer on board the EOS-Terra satellite, which consists of three separate subsystems: the visible and near infrared (VNIR), the short-wave infrared (SWIR) and the thermal infrared (TIR) (Yamaguchi et al., 1998). The TIR subsystem has five spectral channels between 8 and 12 μm with spatial resolution of 90 m (Table 1). The multispectral TIR capability is an exclusive feature of ASTER, which allows the retrieval of land surface temperature (LST) and emissivity spectra at high spatial resolution. Surface temperature and emissivity are critical in the knowledge of the surface energy balance (Ogawa et al., 2003; French et al., 2005). Emissivity spectra provide important information on the mineral composition of land surfaces (Vaughan et al., 2005; Rowan et al., 2005).

LST and spectral emissivities are retrieved from ASTER TIR data by means of the Temperature Emissivity Separation (TES) method (Gillespie et al., 1998). It is applied to at-ground TIR radiances, which have been corrected for atmospheric effects with the ASTER standard atmospheric correction algorithm (Palluconi et al., 1999), and requires the knowledge of the downwelling sky irradiance. The ASTER TIR standard correction algorithm is based on radiative transfer calculation using the MODTRAN code (Berk et al., 1999), with input atmospheric profiles extracted from either the Global Data Assimilation System (GDAS) product or the Naval Research Laboratory (NRL) climatology model. Tonooka (2001, 2005) proposed a water vapor scaling (WVS) method for improving the standard atmospheric correction. The atmospheric water vapor profile is scaled by a factor γ , which is obtained from estimates of surface temperature for gray body pixels and radiative transfer calculations. According to Tonooka (2005), using wavelength-dependent values of factor γ yielded more accurate and physically reasonable estimates of surface temperatures and emissivity spectra than the standard atmospheric correction.

The TES method calculates a normalized temperature and emissivity spectrum by means of the Normalized Emissivity Method (NEM, Gillespie, 1986; Realmuto, 1990). Then, the ratio method (Watson, 1992) is applied to obtain the β spectrum, which preserves the shape of the actual emissivity spectrum but not the amplitude. To obtain the amplitude and thus a better estimate of the LST, the maximum-minimum difference of β (MMD or spectral contrast) is calculated and used to predict the minimum emissivity (ϵ_{\min}) with the aid of an empirical

relationship (Matsunaga, 1994). The accuracy of the TES-derived LST and emissivity depends on the accurate determination of the MMD. Several wavelength-dependent sources of error can affect the MMD, including errors in the calibration of the TIR channels, inaccurate atmospheric correction of at-sensor radiances, and radiometric noise. For gray or near gray bodies (i. e., surfaces with small MMD, such as vegetated surfaces and water bodies), the apparent MMD could be larger than the actual MMD, yielding inaccurate emissivity spectra both in spectral shape and amplitude, and consequently inaccurate LST. A larger MMD implies a lower ϵ_{\min} and thus spectral emissivities are underestimated and LST is overestimated. The problem with near-grey body surfaces in the TES algorithm was recognized by Gillespie et al. (1998). They proposed to consider all pixels with apparent MMD smaller than a given threshold (0.03) as grey bodies, and to assign $\epsilon_{\min}=0.983$ in these cases. The MMD- ϵ_{\min} empirical relationship is only used to calculate ϵ_{\min} when $\text{MMD}>0.03$. Tonooka and Palluconi (2005) evaluated the standard atmospheric correction for the ASTER TIR channels over water surfaces (MMD=0.008). They obtained MMD errors of 0.05 for atmospheric precipitable water of 3 cm, roughly corresponding to surface temperature errors of -0.8 or +2.3 K.

The objective of this study was to analyze the performance of the TES algorithm for the case of low spectral contrast surfaces, such as agricultural areas and water surfaces. We also included a case with high spectral contrast (beach sand). Three ASTER scenes were acquired over a test site close to Valencia, Spain in the summers of 2004 and 2005. The Valencia test site is located in a thermally homogeneous area of rice crops with nearly full vegetation cover in summer, and has been recently used for the validation of satellite-derived LSTs (Coll et al., 2005 and 2006). Ground measurements of surface temperature and emissivity, and atmospheric radiosonde profiles were collected concurrently with ASTER data acquisitions. Based on the results obtained from the comparison with ground data, we propose a scene-based method for adjusting the ASTER TIR radiances with the aim of retrieving reliable emissivity spectra for low spectral contrast surfaces.

The basic concepts of temperature-emissivity separation from TIR data are briefly presented in section 2. Section 3 describes the experimental data used in this study, including the ASTER data and ground measurements. In section 4, ASTER L1B data, LSTs and spectral emissivities are compared with the ground data. In section 5, the method for adjusting the ASTER radiances is presented. Section 6 shows the application of the method and the results obtained in terms of emissivity spectra and LST. Finally, the conclusions are given in section 7.

2. TEMPERATURE AND EMISSIVITY SEPARATION

The at-sensor radiance measured in ASTER TIR channel j ($j=10-14$), $L_{s,j}$, can be related to the LST (T) and emissivity in channel j (ϵ_j) according to

$$L_{s,j} = [\epsilon_j B_j(T) + (1-\epsilon_j) F_{sky,j} / \pi] \tau_j + L_{a,j} \quad (1)$$

where B_j is the Planck function for the effective wavelength of channel j (see Table 1), τ_j is the atmospheric transmittance, $L_{a,j}$ is the atmospheric path radiance emitted towards the sensor, and $F_{sky,j}$ is the downwelling sky irradiance (Lambertian reflection assumed), all for channel j . The term in square brackets in Eq. (1) represents the radiance at ground level, $L_{g,i}$, or “land-leaving” radiance

$$L_{g,j} = \epsilon_j B_j(T) + (1-\epsilon_j) F_{sky,j} / \pi \quad (2)$$

which can be calculated from the at-sensor radiance if the atmospheric parameters τ_j and $L_{a,j}$ are known, i.e.,

$$L_{g,i} = \frac{L_{s,j} - L_{a,j}}{\tau_j} \quad (3)$$

The TES method is applied to the at-ground radiances, Eq. (2), where T and ϵ_j are coupled. For a multispectral TIR sensor with N channels, there will be $N+1$ unknowns (one LST and N spectral emissivities) with only N measurements. In the TES algorithm an empirical relationship between the range of emissivities and the minimum value in the N channels is used to break down the underdeterminacy (Gillespie et al., 1998).

The algorithm uses the NEM module, where the LST is initially estimated as the maximum temperature calculated with the N at-ground radiances using an assumed emissivity value (typically $\epsilon=0.97$) and an estimate of the sky irradiance $F_{sky,j}$ in Eq. (2). With the preliminary LST, an initial estimation of the emissivity in the N channels can be obtained. The first estimates of T and ϵ_j are used in the “ratio” module, where a β -spectrum is calculated as

$$\beta_j = \frac{L_{e,j}}{B_j(T) L_e} \quad (4)$$

where $L_{e,j} = \epsilon_j B_j(T)$ is the radiance emitted by the surface that can be obtained as

$$L_{e,j} = L_{g,j} - (1 - \epsilon_j) F_j^{\text{sky}} / \pi \quad (5)$$

and L_e and B are, respectively, the average of $L_{e,j}$ and $B_j(T)$ for the five ASTER channels. Then, the maximum-minimum difference $MMD = \max(\beta_j) - \min(\beta_j)$ is calculated, which is related to the minimum emissivity, ϵ_{\min} , according to an empirical relationship derived from laboratory spectral measurements of rocks, soils, vegetation, snow, and water (Gillespie et al., 1998):

$$\epsilon_{\min} = 0.994 - 0.687 \times MMD^{0.737} \quad (6)$$

Then, the ϵ_{\min} value is used to calculate the emissivities from the β_j spectrum according to $\epsilon_j = \beta_j \epsilon_{\min} / \min(\beta_j)$ and finally, Eq. (2) is used again with the new emissivity estimates to calculate the LST. In fact, Eq. (2) provides N surface temperatures (one per channel) that should be equal in principle but show small differences in practice. An iterative procedure is suggested using the derived emissivities in the ratio module to reduce the difference between the N temperatures and improve the correction for the downwelling irradiance. However, the differences between the N temperatures are usually below the noise equivalent temperature difference (NEAT) of ASTER (± 0.3 K), so the iterative procedure is not required.

3. EXPERIMENTAL DATA

One of the major problems in the validation of remote sensing data with ground-based measurements is the dissimilarity between the spatial scales of field radiometers (typically $< 1 \text{ m}^2$) and satellite sensors ($90 \times 90 \text{ m}^2$ for ASTER TIR). The comparison of ground (point) measurements with satellite (area-averaged) data is only meaningful when the test site is homogeneous (both in temperature and emissivity) at the various spatial scales involved. On the other hand, ground and satellite data must be as consistent as possible (e.g., same spectral resolution for emissivity comparisons). Finally, the accuracy of the ground measurements must be assessed, including the natural variability of the surface. The ideal validation experiment is very difficult to achieve, water bodies being the most suitable sites (e.g., Hook et al., 2007). Bare soil sites such as dry lakes or “playas” have been also used for ASTER TIR validation/calibration (Tonooka et al., 2005).

Densely vegetated surfaces may be homogeneous enough in temperature and emissivity to serve as validation sites for TIR remote sensing. Emissivity of green vegetation is known to be high and with small spectral

variation (Salisbury and D'Aria, 1992), which facilitates the measurement of temperature by means of field radiometers. The Valencia test site is located in a large extension of rice crops south of Valencia, Spain. In July and August, rice crops are flood-irrigated and show nearly full vegetation cover. Only narrow tracks and irrigation channels cross the site, making the fields accessible and not breaking too much the thermal uniformity. An assessment of the homogeneity of the area at different spatial scales can be found in Coll et al. (2005 and 2006). Further analysis is shown in section 3.1. Figure 1 shows an ASTER VNIR false color image of 36×36 km² including the rice field area (in red) and environs on August 3, 2004.

Ground measurements were carried out at the Valencia site concurrently to three ASTER data acquisitions on August 3 and 12, 2004 and July 21, 2005 (overpass time at around 11:00 UTC). Surface temperatures were measured in the rice fields around the time of the satellite overpass. The measurement site was centered at 39° 15' 01'' N, 0° 17' 43'' W in 2004 and 39° 15' 54'' N, 0° 18' 28'' W in 2005 (see Figure 1). Auxiliary emissivity measurements were performed for the rice crop and a sand sample. With the aim of simulating ASTER L1B radiance data from the field derived surface temperatures, atmospheric radiosondes were launched from the test site. The ASTER data used in this study are shown below. Section 3.2 describes the ground measurements of temperature and emissivity. Section 3.3 shows the local atmospheric data. In section 3.4, other reference data are presented for comparison with ASTER.

3.1. ASTER data

ASTER L1B data (geo-referenced at-sensor radiance), surface kinetic temperature (AST 08) and spectral emissivity (AST05) data products were obtained through the Earth Remote Sensing Data Analysis Center (ERSDAC). For the temperature and emissivity products, atmospheric correction was performed with the ASTER/TIR standard algorithm (Palluconi et al., 1999), using atmospheric profiles from the Global Data Assimilation System (GDAS), and for comparison, climatology from the Naval Research Laboratory (NRL). Figure 2 shows the standard LST product with GDAS atmospheric correction (400×400 TIR pixels) for the same area as in Figure 1.

The thermal homogeneity of the rice field area was assessed at the ASTER scale with the surface temperature product (GDAS atmospheric correction). For each scene, the LST for the pixel closest to the measurement site

was extracted. Arrays of 3×3, 5×5 and 11×11 pixels (1 km²) centered on this pixel were selected for which we calculated the average temperature (T_{av}), the standard deviation (σ), and the minimum and the maximum temperatures (T_m and T_M). Results are shown in Table 2. For all dates and pixel arrays, σ ranged from 0.3 to 0.5 °C and the maximum difference between T_{av} for different arrays in a given date was 0.5 °C. For comparison, the standard deviation for 11×11 pixels over the nearby sea surface ranged from 0.15 to 0.20 °C on the three scenes, and the ASTER NE Δ T is 0.3 °C. For the approximately 4400 pixels (~36 km²) inside the solid line polygon shown in Figure 2 (excluding the built up hot spot in the dashed line square, which is the largest temperature heterogeneity in the area), we obtained $\sigma=0.45$ °C. Maximum temperatures correspond to pixels including narrow tracks or small buildings, which have certain impact at the ASTER spatial resolution. Such pixels could be manually discarded in the comparison with rice ground temperatures. Coll et al (2005 and 2006) studied the thermal homogeneity of the rice field area at the 1 km² scale. Analysis of Terra/Moderate Resolution Imaging Spectrometer (MODIS) LST data (MOD11_L2 product, Wan et al., 2002) showed that $\sigma \leq 0.3$ °C for 3×3 pixels centered on the measurement sites. Similarly, for the more than 30 MODIS pixels contained in the solid line polygon of Figure 2, σ was between 0.2 and 0.3 °C on the three dates. These results show that the thermal homogeneity of the rice field area is quite good both at the ASTER scale ($\sigma \leq 0.5$ °C) and at 1 km² ($\sigma \leq 0.3$ °C).

3.2. Ground measurements

Surface temperature measurements were performed in the rice field area concurrently with each ASTER observation. Two CIMEL 312 four-channel radiometers (channels 1 to 4 at 8-13 μ m, 11.5-12.5 μ m, 10.5-11.5 μ m and 8.2-9.2 μ m, respectively) were used. CIMEL measures the surface-leaving radiance in the four channels consecutively; with one measurement cycle (one measure per channel) lasting 20 s. Other operation mode consists in a cycle of four consecutive measurements for a selected channel, which is used for the emissivity measurements (see below). Radiometers were calibrated against a reference black-body before and after each field measurement, resulting in absolute accuracies better than 0.2 °C in all channels for both instruments. The radiometers were placed about 150 m apart and carried across transects in the rice fields.

Ground temperatures measured within three minutes of the Terra overpass were selected for comparison with the ASTER measurements. This involves 48 temperature measurements (2 radiometers \times 6 cycles \times 4 channels) along two 50-m transects, from which we calculated the average and the standard deviation (~0.5 °C for the three

days). It gives us an estimation of the natural (spatial and temporal) variability of the ground temperatures, mostly due to wind conditions. The three-minute window adopted here is a compromise between sufficient sampling and not introducing too much temporal variability. Radiometric temperatures were corrected for emissivity effects using field measurements of emissivity and downwelling sky irradiance. Together with the average ground LST, an error budget was estimated including the errors in the calibration of the ground radiometers, the emissivity correction and the natural variability of surface temperatures, which was the largest source of error. More details on the ground LST derivation can be found in Coll et al. (2005). Table 3 shows the ground LSTs and uncertainties for the ASTER overpasses on the three days considered.

The emissivity of the rice crops was measured in the field in the four channels of the CIMEL 312 radiometer. We used the box method (Rubio et al. 1997), which can be applied in the field with hand held radiometers and is briefly described here. The inner walls of the box are made with highly reflecting polished aluminum. There are two interchangeable top lids; the “cold” lid of the same material and the “hot” lid made of highly emitting material (corrugated aluminum painted in Parson’s black), which can be heated to about 60 °C. Both lids have a small aperture for the radiometer to observe the radiance coming from the bottom of the box. The bottom can be open or closed with another “cold” lid. The measurement of emissivity with the box methods requires a series of radiance measurements for the sample-box system in different configurations. In the first measurement, the box (bottom open) is placed over the sample, which is at temperature T_s and has emissivity ϵ_s . With the cold lid at top, radiance L^1 is measured. In the second measurement (L^2), the hot lid at temperature T_h is used at top instead of the cold lid. For the third measurement (L^3), the hot lid is still at top but the box is closed with a cold lid at the bottom. In an ideal box, emissivity is 0 for the walls and cold lids and 1 for the hot lid. In this case, the three above measurements are given by (channel dependence omitted for clarity)

$$L^1 = B(T_s) \tag{7a}$$

$$L^2 = \epsilon_s B(T_s) + (1 - \epsilon_s) B(T_h) \tag{7b}$$

$$L^3 = B(T_h) \tag{7c}$$

where B is the Planck function for the channel used. Equations (7a-c) can be solved for ϵ_s as

$$\epsilon_s = \frac{L^3 - L^2}{L^3 - L^1} \tag{8}$$

The series of three measurements takes about 1 minute for each CIMEL channel. Note that T_s must remain constant during measurements of L^1 and L^2 as well as T_h through L^2 and L^3 . With this aim, the walls and lids of the box are externally covered by a 3 cm thick sheet of a thermally insulating material and the hot lid is equipped with a thermostat. Since in equation (8) the error is smaller when the difference L^3-L^1 is larger, a difference $T_h-T_s \geq 30$ °C is recommended. In the real box, typical values of emissivity for the cold and hot lids are 0.03 and 0.98, respectively. Consequently, the contribution of the temperature of the cold lid (T_c) to the measured radiances is not negligible. For these reasons, Eq. (8) is only an approximation to the sample emissivity. A correcting term must be introduced, which requires a fourth measurement (L^4) with cold lids both at top and bottom of the box. Details on the correction for the emissivity measurement are given in Rubio et al. (2003).

A total of 30 emissivity measurements were taken for each CIMEL channel at 3 different spots on the rice fields. Table 4 shows the average emissivity values and uncertainties. The uncertainty is estimated as the maximum between the standard deviation of the 30 measurements and the error resulting from the propagation of measurement uncertainties through Eq. (8). As quoted before, the measured emissivities were used for the correction of the ground radiometric temperatures. Although the CIMEL channels do not match the ASTER TIR channels, our measurements could also be used as a reference for the ASTER derived emissivities over the rice fields. Measurements show high emissivity ($\epsilon > 0.98$) with small spectral variation (< 0.5 %, i.e., comparable to the measurement uncertainties), which is typical for crops with full cover of green vegetation (Salisbury and D'Aria, 1992; Rubio et al., 2003). Therefore, a gray body spectrum with $\epsilon \approx 0.985 \pm 0.005$ (MMD ≈ 0.005) could be assumed for the rice crops.

The box method was also employed for measuring the emissivity of beach sand from the spot shown in Figures 1 and 2. In the field, sand reaches high temperatures thus the condition $T_h-T_s \geq 30$ °C is not met and Eq. (8) is inaccurate. For this reason, a sand sample was taken to the laboratory. We tried not to alter the characteristics of the sample (compaction, grain size distribution, humidity). When the sample was at ambient temperature, the box method was used as in the field. The sand emissivities measured in the CIMEL channels are also given in Table 4. We obtained a low emissivity value for channel 4 (~ 8.7 μm), which is typical for soils rich in quartz (95 % for our sample), and a high spectral contrast (~ 0.13). In the case of sand, the use of CIMEL emissivities for comparison with ASTER is much more problematic (channel 4 covers ASTER channels 10-12, and channel 3 is

similar to ASTER channel 13). We only used the measured sand emissivities as a reference for the ASTER derived MMDs over the sand area.

3.3. Local atmospheric radiosonde and radiative transfer calculations

Atmospheric profiles of pressure, temperature and humidity were measured at the test site concurrently with ASTER overpasses by means of Vaisala RS80 radiosondes. The air temperature at surface level (T_a) and the total column water vapor, or precipitable water (pw), obtained from the radiosonde data for each day are given in Table 3. The atmospheric data were used as inputs to the MODTRAN 4 radiative transfer code (Berk et al., 1999) to simulate the ASTER L1B radiance data from the field derived surface temperatures (section 4.1). The measured radiosonde profiles were completed with mid-latitude summer standard profiles up to 100 km altitude. Rural aerosol model with visibility of 23 km was selected. Atmospheric transmittance, path radiance (both for nadir observation) and downwelling atmospheric radiance ($L_d(\theta)$), for zenith angles from $\theta = 0^\circ$ to $\theta = 85^\circ$ at steps of 5°), were calculated spectrally with MODTRAN 4 and integrated with the response functions of the ASTER TIR channels. The downwelling sky irradiance, $F_{sky,j}$ was obtained from

$$F_{sky,j} = \int_0^{2\pi} d\varphi \int_0^{\pi/2} L_{d,j}(\theta) \cos \theta \sin \theta d\theta \quad (9)$$

where φ is the azimuth angle. The atmospheric parameters τ_j , $L_{a,j}$, $F_{sky,j}/\pi$, and $L_{d,j}(0^\circ)$ (downwelling atmospheric radiance at nadir) calculated for the three days are given in Table 5.

3.4. Other reference data

Water surfaces provide optimum validation conditions for TIR data due to the high homogeneity both in temperature and emissivity. Unfortunately, field measurements were not performed over water surfaces in this work. Other data sources were used as a reference of ASTER TIR products for the case of the sea surface. We used the laboratory-measured emissivity spectrum of sea water from the ASTER spectral library (<http://speclib.jpl.nasa.gov>). It was integrated to the ASTER channels and compared with the channel emissivities derived with TES (section 4.2). We also compared the ASTER surface temperature product with concurrent MODIS sea surface temperature (SST) data at 1 km^2 resolution (MOD28; Brown and Minnett, 1999). Minnett et al. (2004) reported accuracy better than $0.5 \text{ }^\circ\text{C}$ for MODIS SST in comparison with at-sea

measurements of skin SST. MODIS data were acquired through the Earth Observing System Data Gateway (<http://edcimswww.cr.usgs.gov>). Despite the different spatial resolution of ASTER and MODIS, and the different algorithms used for the surface temperature derivation (split-window technique in MOD28), we considered that MOD28 data could be a reasonable reference for ASTER temperatures over the sea surface. Table 3 shows the MOD28 SSTs for 3×3 pixels (average ± standard deviation) centered on 39° 20' 57" N, 0° 3' 44" E (August 3, 2004), 39° 9' 37" N, 0° 4' 41" W (August 12, 2004) and 39° 29' 25" N, 0° 15' 11" W (July 21, 2005). These points are located as far as possible from the shore in order to assure a better homogeneity in the ASTER-MODIS comparison. Due to different ASTER coverage on the three scenes, we could not select the same area for the comparison. The three sites are out of the area displayed in Figure 2.

4. ANALISYS OF ASTER TIR DATA

4.1. Comparison of L1B data

The ground measurements described in the preceding section were used to compare to the ASTER L1B data. At-sensor radiances were simulated for the rice sites by means of Eq. (1) using the measured ground LSTs, assuming an emissivity $\epsilon_j=0.985$ in all channels, and with the field-derived atmospheric parameters (τ_j , $L_{a,j}$, and $F_{sky,j}$) listed in Table 5.

ASTER L1B digital numbers (DN_j) were extracted for 3×3 pixels centered at the measurement site and were converted into at-sensor radiances using the standard Unit Conversion Coefficients (UCC_j , see Table 1) according to

$$L_{s,j} = (DN_j - 1) \times UCC_j \quad (10)$$

Then, the scene-based re-calibration procedure of Tonooka et al. (2003) was applied to the above $L_{s,j}$ in order to obtain the ASTER at-sensor calibrated radiances, $L_{s,j}(c)$. The re-calibration is linear; i.e.

$$L_{s,j}(c) = A_j \times L_{s,j} + B_j \quad (11)$$

Coefficients A_j and B_j are available via website (<http://www.science.aster.ersdac.or.jp/RECAL>), and depend on the date of the scene acquisition and the Radiometric Calibration Coefficient (RCC) version applied to the scene. The re-calibration is aimed to correct for the temporal decline of the detectors responsivity between consecutive changes in the RCC version (Tonooka et al., 2003) and it is necessary for ASTER TIR products with RCC

versions 1.x and 2.x (2.17, 2.18 and 2.20, respectively, for our three scenes). Recent changes in the processing make the re-calibration unnecessary for RCC versions 3.x and higher.

Table 6 shows the comparison between the at-sensor simulated radiances, $L_{s,j}(\text{sim})$, and the calibrated ASTER radiances, $L_{s,j}(\text{c})$, averaged over the 3×3 pixel areas at the rice field sites for the three scenes used in this study. Differences between simulated and ASTER radiances were channel-dependent. The largest differences were in channel 10 (up to 3.0 %) and smallest in channel 13 (0.1 %). These differences are within the range of differences obtained by Tonooka et al. (2005) in a series of vicarious calibration experiments at different test sites, but larger than those reported by Hook et al. (2007) for the Lake Tahoe sites, particularly for channels 10-12. It should be noted that the atmospheric precipitable water was relatively high for all the dates of the present study ($\text{pw} > 2 \text{ cm}$) and this has a significant influence on the channel 10 radiance data.

We can also express the differences in the ASTER data with regard to the ground data in terms of surface temperature. From the ASTER calibrated radiances, $L_{s,j}(\text{c})$, the local atmospheric parameters of Table 5 and $\epsilon_j = 0.985$ for all channels, the surface brightness temperature for channel j can be obtained by

$$T_j = B_j^{-1} \left[\frac{L_{s,j}(\text{c}) - L_{a,j}}{\tau_j \epsilon_j} - \frac{1 - \epsilon_j}{\epsilon_j} \frac{F_{\text{sky},j}}{\pi} \right] \quad (12)$$

where B_j^{-1} is the inverse Planck function. The differences between the ground measured LSTs (from Table 3) and the resulting ASTER brightness temperatures are given in Table 6. Again, the largest differences corresponded to channel 10 (up to 2.5 °C), while channel 13 yielded the best results, with surface temperatures within the error bounds of the ground LSTs for the three days (differences < 0.4 °C).

To show differences between the ground-measured and the ASTER emissivity data, normalized emissivity values were calculated for each ASTER channel using the NEM method. The maximum temperature obtained for channel j from Eq. (12) was assumed to be the actual LST, i.e., $T_{\text{NEM}} = \max(T_j)$ and spectral emissivities were calculated according to

$$\epsilon_j = \frac{L_{g,j} - F_{\text{sky},j} / \pi}{B_j(T_{\text{NEM}}) - F_{\text{sky},j} / \pi} \quad (13)$$

where $L_{g,j}$ is the ASTER radiance at ground level (after atmospheric correction of $L_{s,j}(c)$ with the local atmospheric parameters, Eq. 3). The resulting emissivities are shown in Table 6. While it is not meaningful to directly compare 4-channel field emissivity data from a small area to 5-channel 90-m TIR ASTER emissivity data, the measured MMDs may be compared. According to the field measurements, a realistic MMD would be approximately 0.005. The apparent MMD calculated from the ASTER NEM emissivity data was 0.067, 0.050 and 0.076, respectively, for the three dates studied. However, this difference may be an artifact of the underlying assumptions in the NEM emissivity calculations.

4.2. Validation of ASTER surface temperature and spectral emissivity products

In this section, we show a comparison between ASTER LST and spectral emissivity products (both with GDAS and NRL atmospheric correction) and ground data. Figure 3 shows the average spectral emissivities obtained for 3×3 pixels centered at the rice sites on the three days analyzed, together with the field measurements. Figure 4 shows the average spectral emissivities for the sea surface (33×33 pixels or $3 \times 3 \text{ km}^2$ collocated with the MOD28 data of Table 3).

In the case of low spectral contrast surfaces such as rice and sea, Figures 3 and 4 showed discrepancies between the ASTER-derived emissivities and the measured values, both in terms of magnitude and spectral shape. Spectral variations were larger than expected and emissivities were underestimated. This is a consequence of the ϵ_{\min} -MMD relationship of the TES algorithm (Eq. 6), where higher MMD (higher than the threshold of 0.03) results in lower emissivities. There were also large variations between the results for the same surface on different dates, especially in channels 10-12. For the rice crops, the average MMDs obtained with GDAS atmospheric correction were 0.056, 0.033, and 0.066 for the three dates respectively (0.040, 0.032, and 0.024 with NRL), while MMD=0.005 from the field measurements. For the sea surface, the average MMDs for GDAS were 0.082, 0.052, and 0.087 on the three days respectively (0.047, 0.039, and 0.038 for NRL), while MMD=0.008 from the laboratory spectrum. Emissivities were underestimated in all channels (in channel 10 up to 10 % with GDAS and 6 % with NRL). Channels 13 and 14 showed smaller differences (~2 %). NRL emissivities were somewhat better than GDAS emissivities for the data studied here. Statistically, GDAS is better than NRL (Tonooka and Palluconi, 2005), but it is also natural that NRL shows better results in some cases.

Table 7 shows, for rice and sea, the differences between the ground measured LSTs (MOD28 SST for the sea) and the ASTER derived LSTs, both with GDAS and NRL atmospheric correction. Due to the lower emissivity values in channels 13 and 14 (where the maximum emissivity usually occurs) the derived LSTs were higher than the ground reference temperatures. Contrarily to what happens with emissivity, the best temperature results were obtained by GDAS, with differences not exceeding 1 °C for the three scenes analyzed.

Finally, Figure 5 shows the average spectral emissivities extracted for 4 pixels covering the sand spot in Figures 1 and 2 for the three dates, and the sand emissivity measurements of Table 4. In this case of high spectral contrast surface, there was a better agreement with the field data. The MMDs obtained with GDAS atmospheric correction were 0.143, 0.127, and 0.128 for the three dates respectively (0.137, 0.114, and 0.100 with NRL).

5. LOCAL ADJUSTMENT OF ASTER TIR DATA

The results of the previous section show inaccuracies in the retrieved emissivity spectra and thus in the estimated LSTs. Possible causes include miscalibration of the TIR channels, errors in the atmospheric correction (near sea level there is more water vapor to correct for), and propagation of radiometric noise. All these effects are wavelength-dependent, which could yield inaccurate MMDs, particularly for low spectral contrast surfaces. It is difficult to know the individual contribution of each source of error. The vicarious calibration experiments reported in Tonooka et al (2005) showed that channels 10-12 have a larger uncertainty. It is also recognized that atmospheric correction in channels 10-12 is more sensitive to errors in the water vapor profile. However, in the present study, channel 13 yielded a good agreement with the ground data, with derived surface temperatures within the error bounds of the ground LSTs (Table 6).

In this section, a method to adjust the at-sensor TIR radiances is proposed taking advantage of the good performance of channel 13. The objective of the method is to derive emissivity and LST values from ASTER data that are physically realistic, particularly for low spectral contrast materials. With this aim, we assume that the calibration and the atmospheric correction using the local radiosonde data is accurate for channel 13 over the dynamic range of the scene. We also assume that the scene contains several targets with well known emissivities at different temperatures, which is partly similar to a gray pixel algorithm (Tonooka et al., 1997). Water bodies

(emissivity from ASTER spectral library) are ideal targets, but fully vegetated surfaces with gray-body spectra (i.e., $\epsilon_j=0.985$ in all channels) are also required for a wider temperature range.

The “gray-body adjustment method” starts by selecting several gray-body targets whose temperatures cover as much of the temperature range of the scene as possible. The scene-based re-calibration of Tonooka et al. (2003) is applied. For these targets, the surface temperature is calculated for channel 13 using the local atmospheric parameters of Table 5 and the known emissivity value ($\epsilon_{13}=0.992$ for water; $\epsilon_{13}=0.985$ for full vegetation cover) in Eq. (12). (For water targets, reflection of sky downwelling radiance is specular rather than Lambertian. In these cases, $F_{sky,j}/\pi$ was replaced by the downwelling atmospheric radiance at nadir, $L_{d,j}(0^\circ)$, which is also given in Table 5.) The surface temperature calculated for channel 13 is assumed to be true and used to simulate the radiance at the ground level, $L_{g,i}$, in the other ASTER TIR channels according to Eq. (2) with the local atmospheric parameters ($F_{sky,j}/\pi$ for land targets and $L_{d,j}(0^\circ)$ for water targets) and the known emissivities.

For the Valencia scenes, four targets were selected: the sea surface (lowest temperature), rice crops at the test site, a golf course and a closed pine forest (highest temperature). The locations of the two latter sites are indicated in Figures 1 and 2. Typically 5-10 pixels were selected for each site. In Figure 6, the simulated at-ground radiances are plotted against the original ASTER DN_j for channels 10-14 for the August 3, 2004 scene. The x-axis error bars in Figure 6 correspond to the standard deviation of the digital numbers extracted for each site (~4 DN), and the y-axis error bars correspond to an error of ± 0.5 °C in ground LST and ± 0.005 in emissivity, but do not include the errors of the local atmospheric parameters.

Figure 6 shows a linear relationship between the simulated at-ground radiances and ASTER DN_j , which is also observed for the other scenes, with coefficients of determination $r^2 > 0.99$ for all channels. Therefore we propose a linear, scene dependent adjustment for obtaining the at-ground ASTER radiances from the at-sensor DN_j according to

$$L_{g,j}(\text{adj}) = \alpha_j \times DN_j + \beta_j \quad (14)$$

The coefficients of Eq. (14) and r^2 are given in Table 8 for all channels and scenes. The linear relationship of Eq. (14) implicitly includes the calibration of the ASTER TIR channels (linear conversion from DN_j to radiances, Eq. 10, and linear re-calibration, Eq. 11), and the atmospheric correction of at-sensor radiances (Eq. 3, which is

also linear). Thus adjusted at-ground radiances, $L_{g,j}(\text{adj})$, can be directly obtained from ASTER digital numbers using Eq. (14), from which temperature and spectral emissivity can be derived with the TES method.

6. RESULTS AND DISCUSSION

In this section the TES algorithm was applied to the adjusted at-ground ASTER radiances. In the NEM module of TES, we selected $\epsilon=0.99$ as a first guess, which is appropriate as a maximum emissivity for near-gray bodies. On the other hand, no iteration was made in the first estimation of ϵ_j and LST for the correction of the downwelling irradiance. Finally, according to Gillespie et al. (1998) we set a threshold in the calculated MMD ($\text{MMD}_T=0.03$) to differentiate low and high spectral contrast pixels. If the apparent MMD was larger than MMD_T , ϵ_{\min} was calculated by means of the standard ϵ_{\min} -MMD relationship (Eq. 6). If the calculated MMD is smaller than MMD_T , Eq. (6) is not used and the spectral emissivities and LST retrieved in the NEM module are considered as the final values and the processing is terminated. It implies that the minimum emissivity is given for these cases by $\epsilon_{\min}=0.99-\text{MMD}$, which yields higher estimates of ϵ_{\min} than the standard relationship and introduces less discontinuity than taking a constant value ($\epsilon_{\min}=0.983$).

The need for a threshold in MMD is due, in part, to the propagation of the radiometric noise in the emissivity retrieval, which tends to increase the apparent MMD and can not be corrected with the adjustment equations proposed here. To evaluate the effect of radiometric noise, we simulated at-sensor radiances for a grey body ($\epsilon=0.99$ and $\text{MMD}=0$) at different surface temperatures and converted the radiances into ASTER digital numbers. Noise was added to the simulated radiances in all channels by means of a random number generator between ± 4 DN (roughly equivalent to ± 0.3 °C). Then, radiances were used in TES to derive the spectral emissivities and the apparent MMD was calculated. From these calculations, we found an average $\text{MMD}=0.026\pm 0.011$ for surface temperature of 20 °C, and $\text{MMD}=0.015\pm 0.005$ for surface temperature of 30 °C. These results show a significant increase in the apparent MMD that would yield excessively underestimated values for ϵ_{\min} if the standard relationship was used.

Figure 7 shows an image of MMD calculated with the adjusted at-ground radiances for part of the scene on August 3, 2004. Figure 8 shows the corresponding histogram of the MMD distribution and, for comparison, the MMD obtained from the standard products (both with GDAS and NRL atmospheric correction) for the same area. About 89 % of the pixels yielded $\text{MMD}<0.03$ for the adjusted data, while it was only 6 % for the standard

products. In Figure 7, the large dispersion of MMDs for the sea surface is apparent (scan line noise), taking values from 0.002 to 0.066 (i.e., covering a considerable part of the range of the image) with a mean MMD of 0.023. The rice field area shows relatively low MMDs (from 0.001 to 0.041 and a mean value of 0.013). MMDs for Valencia downtown range between 0.007 and 0.045, with a mean of 0.023. High spectral contrast pixels (typically >0.05) mainly correspond to the sandy coastline and industrial areas in the suburbs of Valencia and other urban areas.

Figure 9 shows a false color image of emissivity retrieved with the TES algorithm for the adjusted radiances of the August 3, 2004 scene. It covers the same area as in Figures 1, 2, and 7 and displays emissivity in channels 10, 12 and 14 in RGB, respectively. For the rice crop area (in white and pink), the image shows high values in all channels. The sea surface is dominated by scan line noise. A high variability is observed with some pixels having low emissivities in channel 10 (in green and blue) while others yielding more reliable values (white). The sandy coastline and some inland spots appear in blue and dark blue, indicating low emissivity values in channels 10 and 12.

Figure 10 shows the spectral emissivities for rice, sea and sand (the same pixels as in section 4.2) for the three scenes analyzed. For rice and sea, spectral emissivities were in good agreement with the measurements. Considering all channels and dates, the difference between ground and derived emissivities ranged between -0.3 and 0.9 % for rice, and between 0.6 and 2.2 % for sea pixels. The derived surface temperatures were also close to the ground measurements for rice: differences (ground minus ASTER) of -0.3, -0.3 and 0.2 °C were obtained for the three dates respectively. In the case of the sea surface, the differences between the concurrent MOD28 SST and the ASTER derived temperatures were 0.3, -0.2 and 0.0 °C for the three dates respectively. The average MMD ranged between 0.009 and 0.016 for the rice crop on the three dates, and between 0.017 and 0.026 for the sea pixels (lowest values for August 12, 2004). These MMDs were around 0.01-0.02 higher than expected (≈ 0.005 for the rice crop and 0.008 for the sea surface), which is a consequence of noise as discussed above. Besides the increase of the MMD, noise effects are apparent in the dispersion of the retrieved emissivities, particularly over the sea surface (see Figure 9). For the 33×33 sea pixels selected, the standard deviation of the calculated MMD was 0.008 for the three dates, with a considerable fraction of pixels exceeding the 0.03 threshold. As a result, the sea water emissivities were somewhat underestimated.

Figure 10 also shows the spectral emissivities obtained for sand, with high spectral contrast. The calculated MMDs were 0.11-0.12 for the three dates, for which the standard ϵ_{\min} -MMD relationship (Eq. 6) yields minimum emissivities of 0.85-0.86. The emissivity measurements for sand showed a minimum emissivity of 0.81, which is lower than predicted by Eq. (6). As a consequence, the emissivities retrieved for sand show higher values than the measurements at all wavelengths.

7. SUMMARY AND CONCLUSIONS

The performance of ASTER TIR products was evaluated for low spectral contrast surfaces. Three ASTER scenes were acquired over a test site close to Valencia, Spain where ground data were concurrently collected. Ground measurements included surface temperature, emissivity, and atmospheric radiosonde profiles. The test site is located in a rice crop area with nearly full vegetation cover in summer. Using the ground data and the local radiosonde profiles, at-sensor radiances were simulated for the ASTER TIR channels and compared with the ASTER L1B data (calibrated at-sensor radiances). The comparison showed discrepancies up to 3 % in radiance for channel 10 (equivalently, 2.5 °C in temperature or 7 % in emissivity), which is the channel most influenced by atmospheric water vapor. Channels 13 and 14 yielded a closer agreement (-0.1% radiance difference).

We also compared the ASTER LST and spectral emissivity data products generated with the TES algorithm to field-derived temperature and emissivity measurements of the rice crops. For the sea surface, ASTER TES products were compared to the MODIS sea surface temperature data product, and for sea surface emissivity, to known lab-measured emissivity of water. Both the GDAS and NRL atmospheric correction options were also compared for ASTER LST and emissivity data products. For rice crop pixels, ASTER showed anomalously low emissivity values at all wavelengths (as much as 8% lower in channel 10 and ~2% lower in channel 13) and larger MMDs than expected (0.033-0.066 for GDAS and 0.024-0.038 for NRL), and consequently overestimated LSTs (by 0.2 to 1.1 °C for GDAS and 0.9 to 2.0 °C for NRL). Results were similar for sea water pixels: MMDs of 0.052-0.087 for GDAS and 0.038-0.047 for NRL, with temperatures exceeding concurrent MOD28 SSTs. Possible reasons for anomalously large MMDs over low-spectral contrast targets include: 1) inaccuracy in the instrument calibration, 2) imperfect atmospheric correction (not accounting for all the water vapor in the column or errors in the radiative transfer model used), 3) inaccuracy in the calibration of the field instruments (for the rice and sand measurements), and the MODIS instrument and data product generation (for the water

measurements), 4) heterogeneity in the surface validation targets at the scale of ASTER, or 5) problem with the TES algorithm classifying radiometric noise as real spectral contrast. The latter issue has a significant impact on the extraction of temperature and emissivity information because TES relies on an empirical relationship between the emissivity minimum and the MMD.

In this work, a scene-based procedure is proposed to adjust the ASTER TIR data in order to obtain more accurate MMD estimates and therefore a better retrieval of LST and emissivity with the TES algorithm. The method uses various gray-bodies or near gray-bodies with known emissivities at different temperatures (e.g., water bodies and fully vegetated surfaces) and assumes that the calibration and atmospheric correction performed with local radiosonde data is accurate for ASTER channel 13. Taking the temperature derived for channel 13 as the true LST, the ASTER TIR radiances corresponding to the gray bodies were simulated for the other channels and used to derive linear relationships between the ASTER digital numbers and the at-ground radiances for each channel.

Using the adjusted radiances, the TES algorithm was applied to derive surface emissivities and LSTs. The products resulting from the adjusted radiances showed a better agreement with the ground measurements and a good stability along the three dates analyzed. For all channels and dates, retrieved emissivities differed from the measured values by -0.3-0.9 % for rice, and by 0.6-2.2 % for sea pixels, while temperatures agreed with the ground values within ± 0.3 °C in all cases. The radiometric noise increased the apparent MMD by 0.01-0.02, an effect that was rather noticeable for homogeneous, low spectral contrast areas in the emissivity and MMD images. For this reason, a MMD threshold of 0.03 was used in the processing of TES that discriminates between low and high spectral contrast pixels. Although the number of scenes analyzed is not statistically significant, the results shown in this study prove the feasibility of retrieving accurate estimates of surface emissivity and its spectral variation with ASTER TIR data for low spectral contrast surfaces.

ACKNOWLEDGEMENTS

This work was funded by the *Ministerio de Educación y Ciencia* (Project CGL2004-06099-C03-01, co-financed with European Union FEDER funds, *Acciones Complementarias* CGL2005-24207-E/CLI and CGL2006-27067-E/CLI), and *Juan de la Cierva* Research Contract of R. Niclòs, and the University of Valencia (*V Segles* Research Grants of J. M. Sánchez and M. Mira). We thank the ASTER Science Team for support and assistance, and *Centro de Estudios Ambientales del Mediterraneo* (CEAM) for the radiosonde data.

REFERENCES

- Berk, A., G. P. Anderson, P. K. Acharya, J. H. Chetwynd, L. S. Bernstein, E. P. Shettle, M. W. Matthew, and S. M. Adler-Golden (1999), MODTRAN 4 user's manual. Air Force Research Laboratory, Space Vehicles Directorate, Air Force Materiel Command, Hascom AFB, MA, 95 pp.
- Brown, O. B., and P. J. Minnet (1999), MODIS infrared sea surface temperature algorithm – Algorithm Theoretical Basis Document, Product MOD28. ATBD reference number MOD-25.
- Coll, C., V. Caselles, J. M. Galve, E. Valor, R. Niclòs, J. M. Sánchez and R. Rivas (2005), Ground measurements for the validation of land surface temperatures derived from AATSR and MODIS data, *Remote Sensing of Environment*, 97, 288-300.
- Coll, C., V. Caselles, J. M. Galve, E. Valor, R. Niclòs, and J. M. Sánchez (2006), Evaluation of split-window and dual-angle correction methods for land surface temperature retrieval from Envisat/AATSR data, *Journal of Geophysical Research*, 111, D12105, doi:10.1029/2005JD006830.
- French, A.N., F. Jacob, M.C. Anderson, W.P. Kustas, W. Timmermans, A. Gieske, Z. Su, H. Su, M.F. McCabe, F. Li, J. Prueger, and N. Brunsell (2005). Surface energy fluxes with the Advanced Spaceborne Thermal Emission and Reflection radiometer (ASTER) at the Iowa 2002 SMACEX site (USA). *Remote Sensing of Environment*, 99, 55 – 65.
- Gillespie, A.R. (1986). Lithologic mapping of silicate rocks using TIMS, in The TIMS Data Users' Workshop, JPL Publication 86-38, Jet Propulsion Laboratory, Pasadena, CA, pp. 29-44.
- Gillespie, A. R., T. Matsunaga, S. Rokugawa, and S. J. Hook (1998). Temperature and emissivity separation from Advanced Spaceborne Thermal Emission and Reflection Radiometer (ASTER) images, *IEEE Transactions on Geoscience and Remote Sensing*, 36, 1113-1125.
- Hook S. J., R. G. Vaughan, H. Tonooka and S. G. Schladow (2007). Absolute Radiometric In-Flight Validation of Mid and Thermal Infrared Data from ASTER and MODIS Using the Lake Tahoe CA/NV, USA Automated Validation Site, *IEEE Transactions on Geoscience and Remote Sensing*, (in press).
- Matsunaga, T. (1994). A temperature-emissivity separation method using an empirical relationship between the mean, the maximum and the minimum of the thermal infrared emissivity spectrum, *Journal of the Remote Sensing Society of Japan*, 14(2), 230-241.
- Minnett, P. J., Brown, O. B., Evans, R. H., Key, E. L., Kearns, E. J., Kilpatrick, K., Kurnar, A., Maillet, K.A., Szczodrak, G. (2004). Sea-surface temperature measurements from the Moderate-Resolution Imaging

- Spectroradiometer (MODIS) on Aqua and Terra, IEEE International Geoscience and Remote Sensing Symposium Proceedings IGARSS 2004, vol. 7, 4576-4579.
- Ogawa, K., Schmugge, T., Jacob, F., French, A. (2003). Estimation of land surface window (8-12 μm) emissivity from multi-spectral thermal infrared remote sensing - A case study in a part of Sahara Desert, *Geophysical Research Letters*, 30 (2), pp. 39-1.
- Palluconi, F., Hoover, G., Alley, R., Jentoft-Nielsen, M., and Thompson, T. (1999). An atmospheric correction method for ASTER thermal radiometry over land, ASTER Algorithm Theoretical Basis Document, revision 3, Jet Propulsion Laboratory, Pasadena, CA.
- Realmuto, V. J. (1990). Separating the effects of temperature and emissivity: Emissivity spectrum normalization, In *Proceedings of the 2nd TIMS Workshop*, JPL Publication 90-55, Jet Propulsion Laboratory, Pasadena, CA, pp. 23-27.
- Rowan, L. C., J. C. Mar, and C. J. Simpson (2005). Lithologic mapping of the Mordor, NT, Australia ultramafic complex by using the Advanced Spaceborne Thermal Emission and Reflection Radiometer (ASTER). *Remote Sensing of Environment*, 99, 105 – 126.
- Rubio, E., Caselles, V., Coll, C., Valor, E. and Sospedra, F. (2003). Thermal-infrared emissivities of natural surfaces: Improvements on the experimental set-up and new measurements. *International Journal of Remote Sensing*, 24 (24), 5379-5390.
- Salisbury, J. W. and D'Aria, D. M. (1992). Emissivity of terrestrial materials in the 8-14 μm atmospheric window. *Remote Sensing of Environment*, 42, 83-106.
- Tonooka, H. (2001). An atmospheric correction algorithm for thermal infrared multispectral data over land - A water-vapor scaling method, *IEEE Transactions on Geoscience and Remote Sensing* 39 (3), 682-692
- Tonooka, H. (2005). Accurate atmospheric correction of ASTER thermal infrared imagery using the WVS method. *IEEE Transactions on Geoscience and Remote Sensing*, 43, 2778-2792.
- Tonooka, H., Rokugawa, S. and Hoshi, T. (1997). Simultaneous estimation of atmospheric correction parameters, surface temperature and spectral emissivity using thermal infrared multispectral scanner data, *Journal of the Remote Sensing Society of Japan*, 17(2), 19-33.
- Tonooka, H., F. Sakuma, M. Kudoh, and K. Iwafune (2003). ASTER/TIR calibration status and user-based recalibration. *Proceedings of SPIE*, vol. 5234, 191-201.
- Tonooka, H., F. D. Palluconi, S. J. Hook, and T. Matsunaga (2005). Vicarious calibration of ASTER thermal infrared channels. *IEEE Transactions on Geoscience and Remote Sensing*, 43, 2733-2746.

- Tonooka, H. and Palluconi, F. D. (2005). Validation of ASTER/TIR standard atmospheric correction using water surfaces. *IEEE Transactions on Geoscience and Remote Sensing*, 43, 2769-2777.
- Vaughan, R. G., S. J. Hook, W. M. Calvin, and J. V. Taranik (2005). Surface mineral mapping at Steamboat Springs, Nevada, USA, with multi-wavelength thermal infrared images. *Remote Sensing of Environment*, 99, 140 – 158.
- Wan, Z., Zhang, Y., Zhang, Q. and Li, Z.-L. (2002). Validation of the land-surface temperature products retrieved from Terra Moderate Resolution Imaging Spectroradiometer data. *Remote Sensing of Environment*, 83, 163-180.
- Watson, K. (1992). Spectral ratio method for measuring emissivity, *Remote Sensing of Environment*, 42, 113-116.
- Yamaguchi, Y., Kahle, A. B., Tsu, H., Kawakami, T., and Pniel, M. (1998). Overview of Advanced Spaceborne Thermal Emission and Reflection Radiometer (ASTER). *IEEE Transactions on Geoscience and Remote Sensing*, 36, 1062-1071.

FIGURES

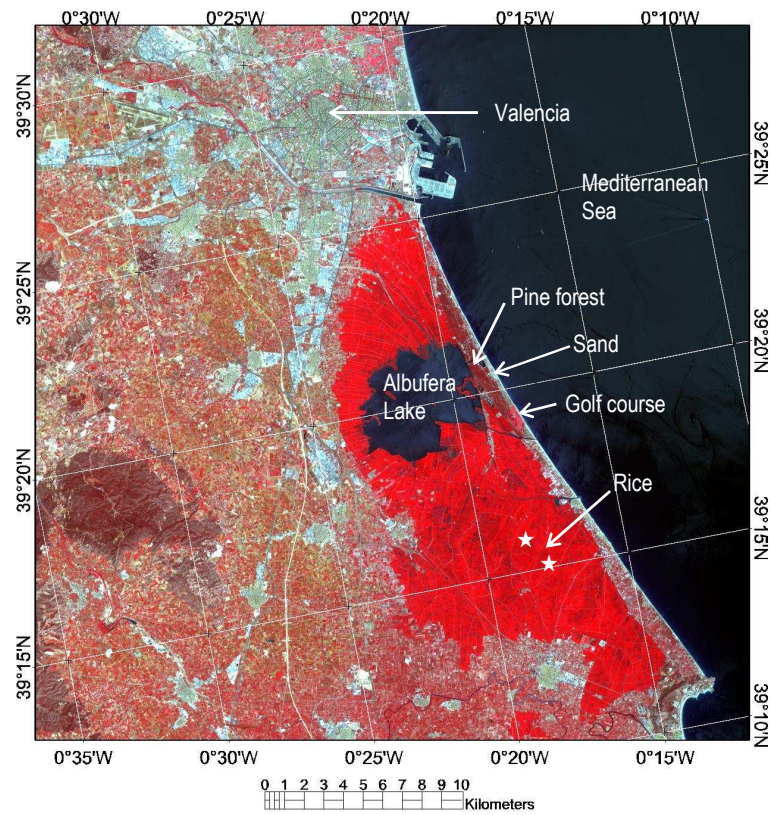


Figure 1. ASTER L1B VNIR image covering the study zone on August 3, 2004. The stars show the location of the rice sites. Other sites mentioned in the paper are indicated. The RGB components are channels 3 (0.81 μm), 2 (0.66 μm) and 1 (0.56 μm), respectively, with 15 m resolution.

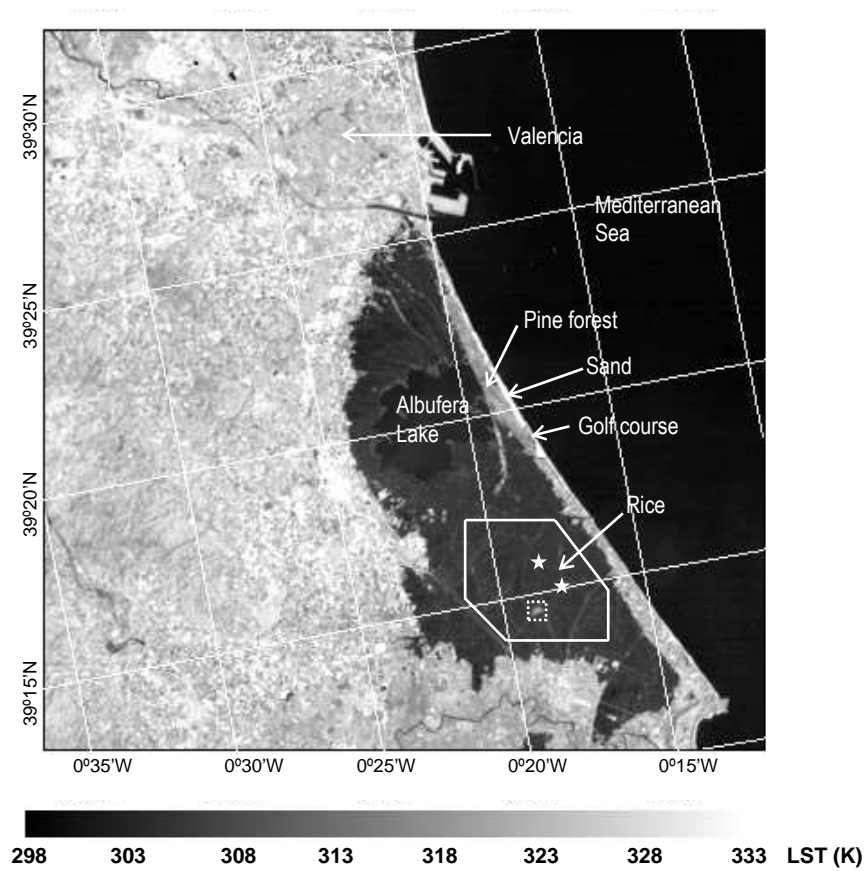


Figure 2. ASTER (AST08) surface kinetic temperature data product (GDAS atmospheric correction) for the same area and date as in Figure 1, with 90-m spatial resolution.

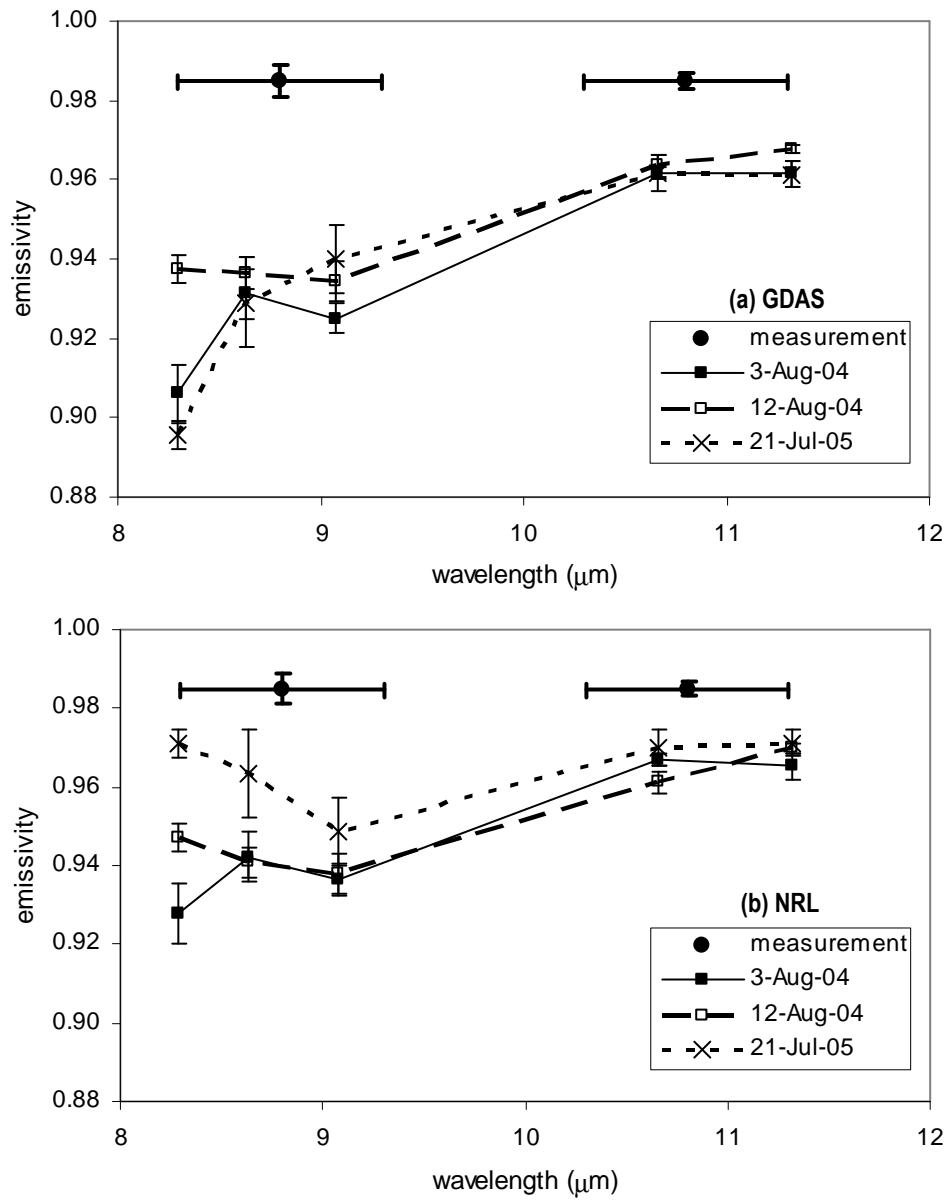


Figure 3. ASTER TES emissivity data for the rice sites with (a) GDAS and (b) NRL atmospheric correction for the three dates indicated. The average values for 3×3 pixels over the site are shown, with one standard deviation as error bar. For the field measurements, the horizontal bars show the width of CE312 channels.

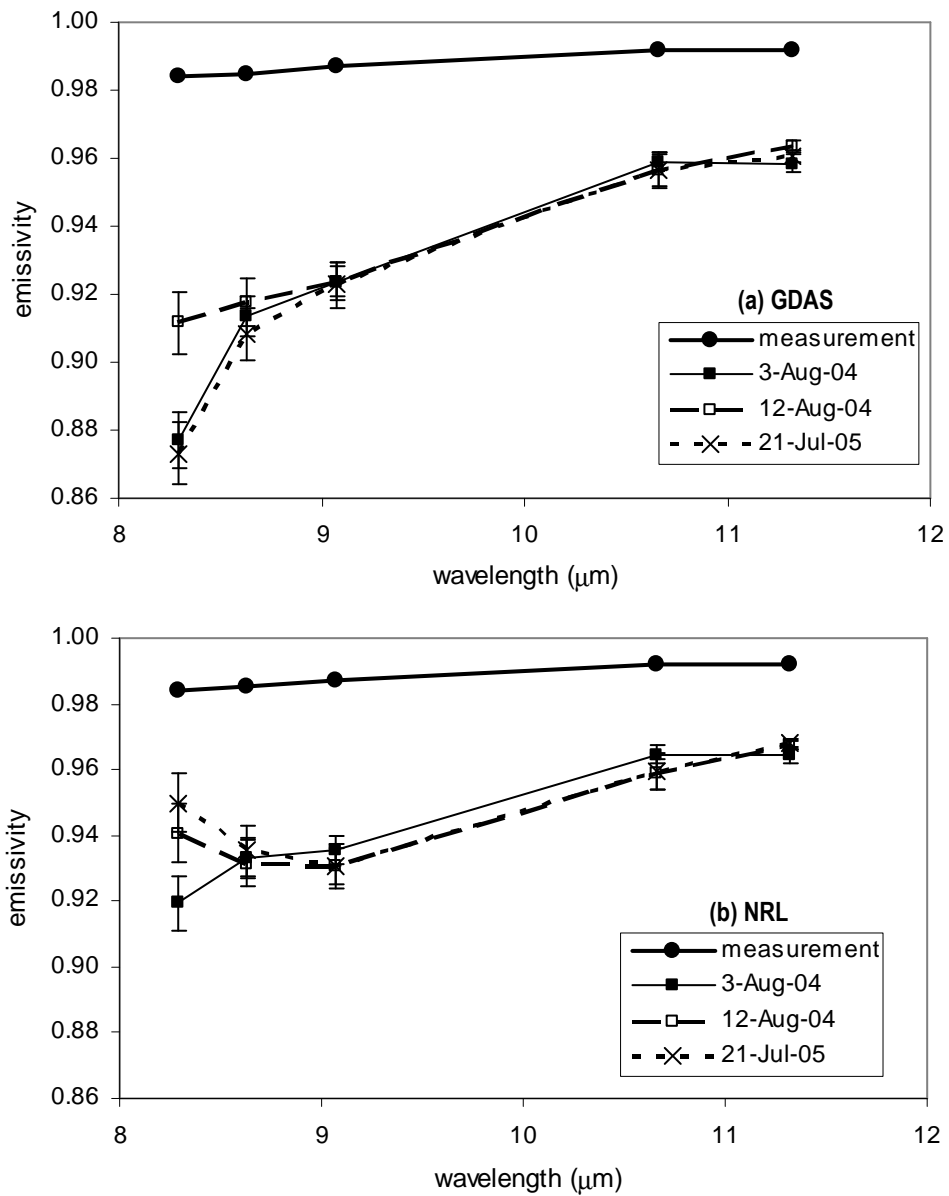


Figure 4. ASTER TES emissivity data for the sea surface with (a) GDAS and (b) NRL atmospheric correction for the three dates indicated. The average values for 33×33 pixels are shown, with one standard deviation as error bar. Measurement refers to the seawater emissivity spectrum from the ASTER library integrated to the ASTER TIR bands.

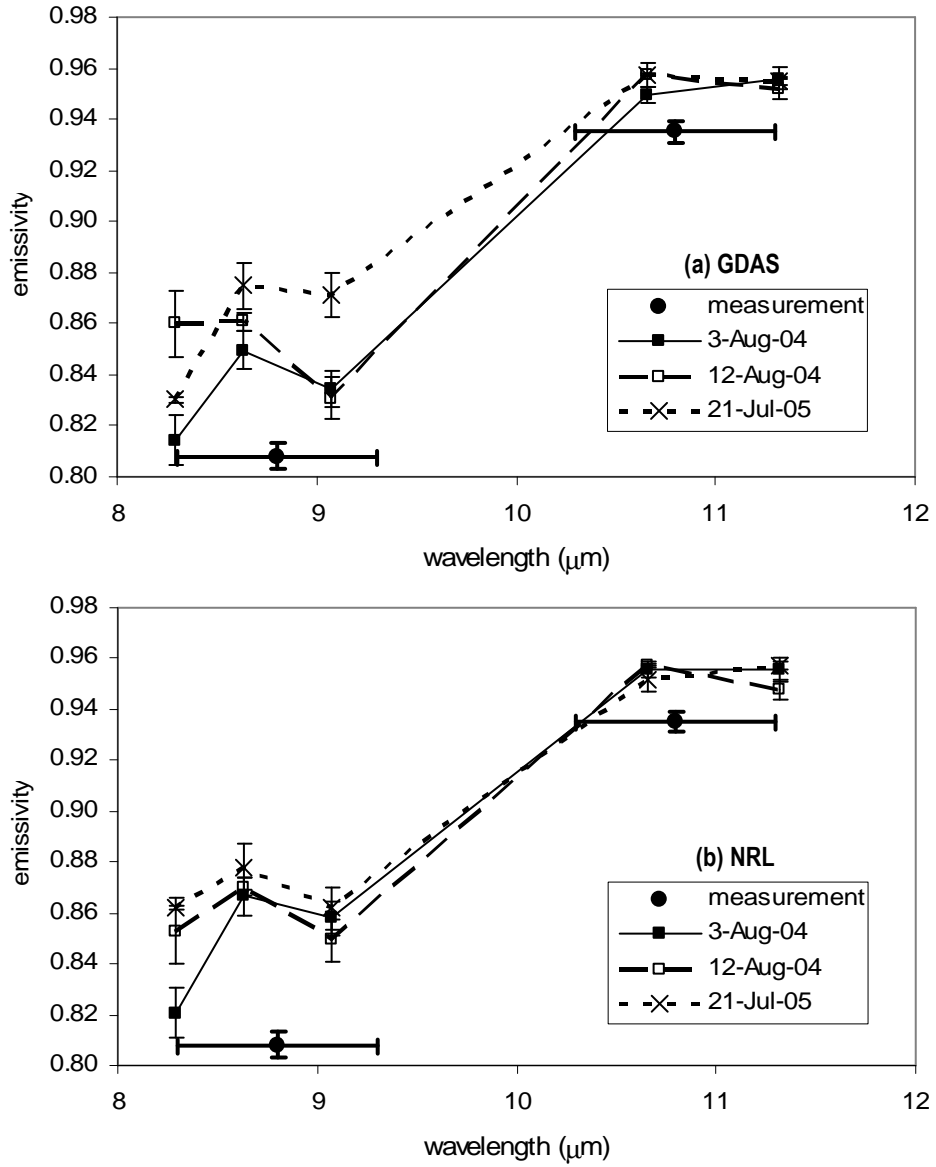


Figure 5. ASTER TES emissivity data for beach sand with (a) GDAS and (b) NRL atmospheric correction for the three dates indicated. The average values for 4 pixels over the site are shown, with one standard deviation as error bar. For the field measurements, the horizontal bars show the width of CE312 channels.

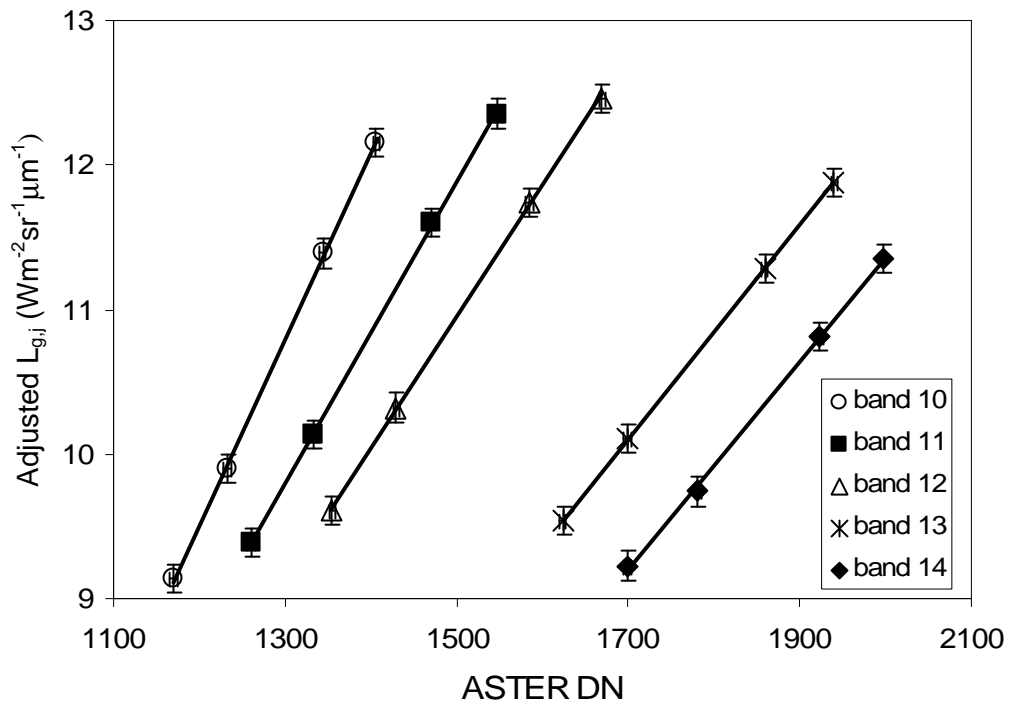


Figure 6. Relationship between the ASTER digital numbers (DN) and the simulated at-ground radiances for the four near gray-body targets in channels 10-14 on August 3, 2004.

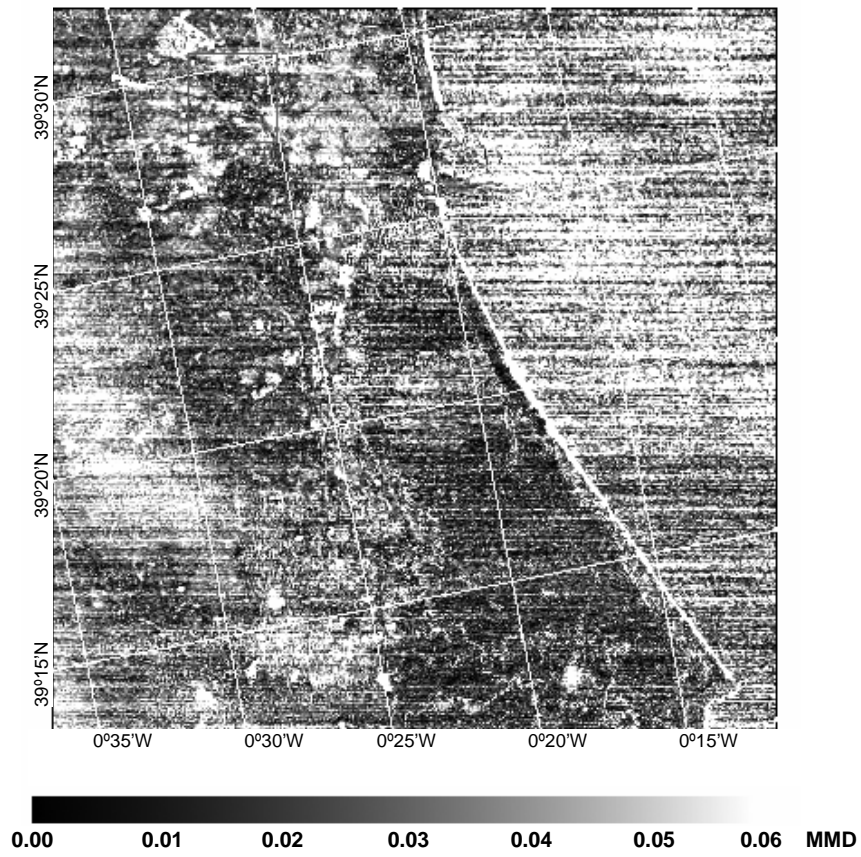


Figure 7. Image of MMD calculated with the adjusted radiances for the same area and date as in Figures 1 and 2.

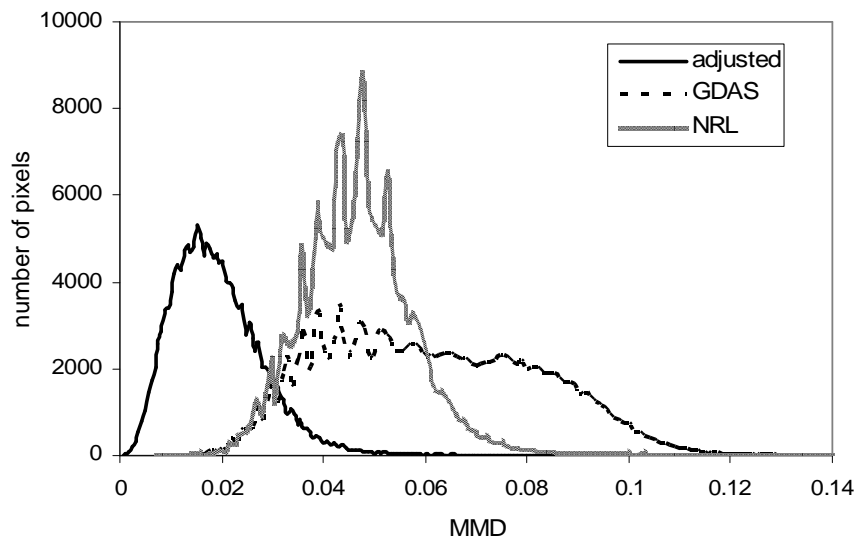


Figure 8. Histogram of the MMD distribution for the image of Figure 7 and for the standard product (GDAS and NRL) corresponding to the same area.

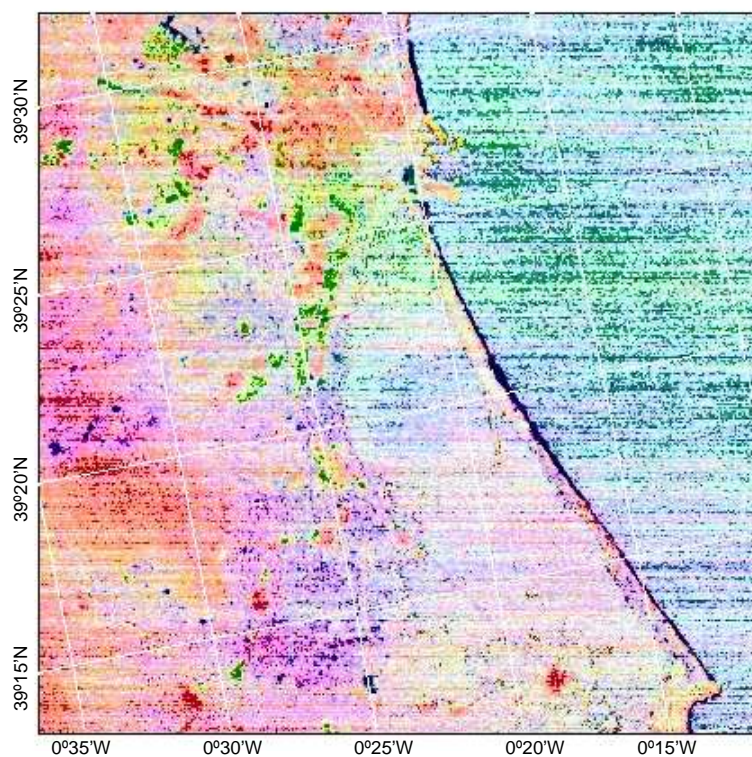


Figure 9. False color composite image of surface emissivity (channels 10, 12 and 14 in RGB, respectively) retrieved with the TES algorithm with adjusted radiances for the August 3, 2004 scene.

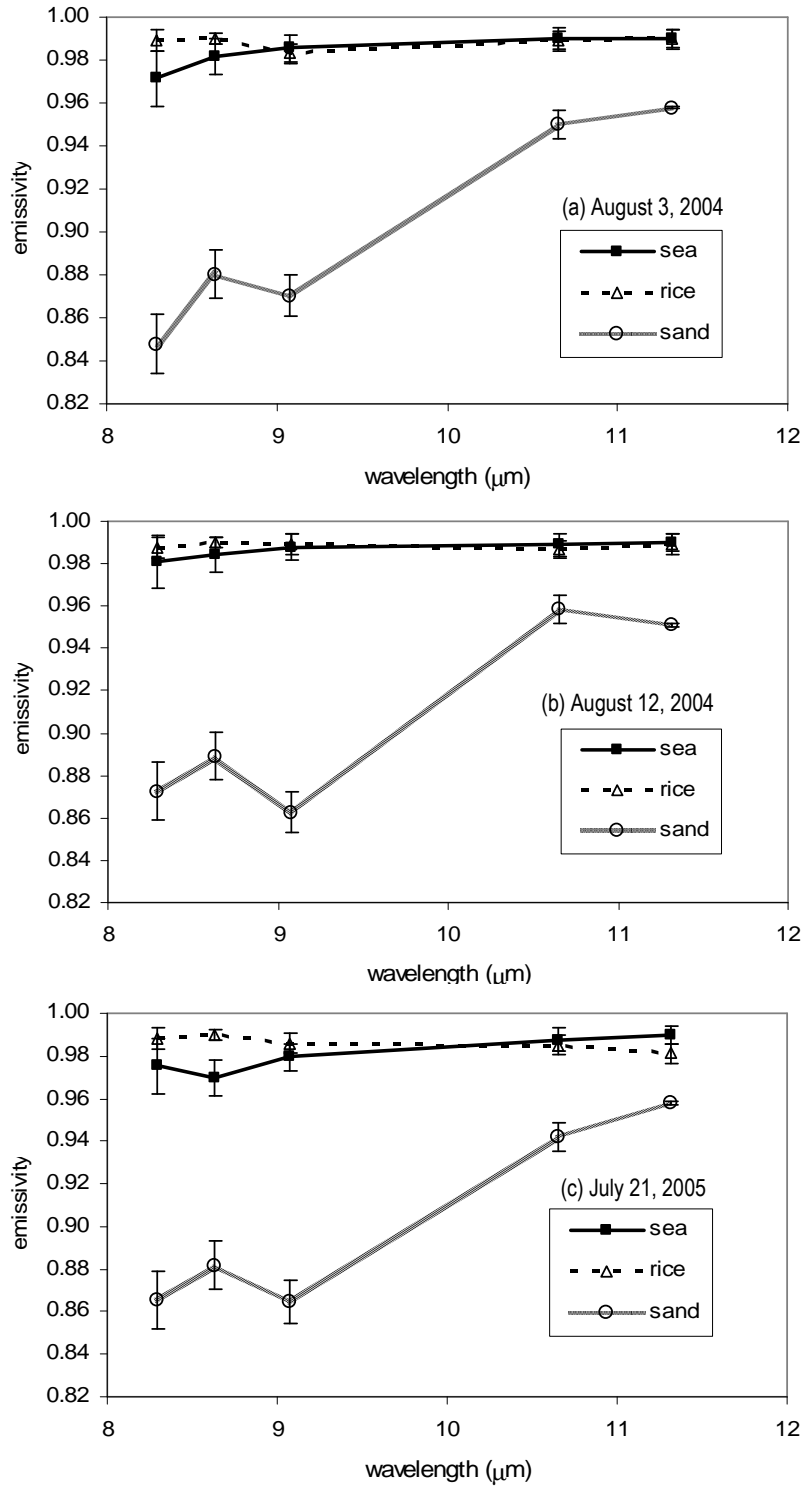


Figure 10. Spectral emissivity retrieved with TES applied to adjusted at-ground radiances for sea, rice and sand on (a) August 3, 2004; (b) August 12, 2004; and (c) July 21, 2005.

TABLES

Table 1. Bandpasses and effective wavelengths of the ASTER TIR channels. The last column gives the Unit Conversion Coefficient (UCC_j) for each channel.

Channel	Bandpass (μm)	Effective wavelength (μm)	UCC_j ($\text{Wm}^2\text{sr}^{-1}\mu\text{m}^{-1}/\text{DN}$)
10	8.125 – 8.475	8.291	0.006882
11	8.475 – 8.825	8.634	0.006780
12	8.925 – 9.275	9.075	0.006590
13	10.25 – 10.95	10.657	0.005693
14	10.95 – 11.65	11.318	0.005225

Table 2. Surface temperature product (GDAS atmospheric correction) for 1×1 , 3×3 , 5×5 and 11×11 pixels on the three dates. T_{av} is the average temperature, σ is the standard deviation, T_m is the minimum temperature and T_M is the maximum temperature.

		T_{av} ($^{\circ}\text{C}$)	σ ($^{\circ}\text{C}$)	T_m ($^{\circ}\text{C}$)	T_M ($^{\circ}\text{C}$)
August 3, 2004	1x1	31.35	-	-	-
	3x3	31.66	0.38	31.25	32.15
	5x5	31.91	0.42	31.25	32.85
	11x11	31.85	0.49	30.75	33.35
August 12, 2004	1x1	29.85	-	-	-
	3x3	29.85	0.28	29.55	30.35
	5x5	30.01	0.36	29.45	30.95
	11x11	29.88	0.50	28.55	31.25
July 21, 2005	1x1	28.65	-	-	-
	3x3	29.04	0.42	28.65	29.75
	5x5	28.91	0.31	28.55	29.75
	11x11	28.82	0.33	28.15	29.85

Table 3. Ground measured LST and uncertainty for the rice sites concurrent with ASTER observations. The third column gives the air temperature at surface level (T_a) and the total precipitable water (pw) from the radiosonde data. The last column shows the MOD28 SST product for 3×3 sea pixels.

Date and overpass time (UTC)	Ground LST $\pm \sigma$ ($^{\circ}\text{C}$)	T_a ($^{\circ}\text{C}$) / pw (cm)	MOD28 SST $\pm \sigma$ ($^{\circ}\text{C}$)
August 3, 2004; 11:00	30.4 ± 0.7	35.0 / 2.35	26.3 ± 0.2
August 12, 2004; 10:54	28.8 ± 0.5	32.0 / 2.05	26.7 ± 0.2
July 21, 2005; 11:00	28.4 ± 0.6	27.2 / 2.03	26.9 ± 0.2

Table 4. Emissivity values for the rice crop and beach sand measured with the four channels of CIMEL 312.

	Ch. 4 (8.2-9.2 μm)	Ch. 3 (10.5-11.5 μm)	Ch. 2 (11.5-12.5 μm)	Ch. 1 (8-13 μm)
Rice crop	0.985 ± 0.004	0.985 ± 0.002	0.980 ± 0.005	0.983 ± 0.003
Sand (beach)	0.808 ± 0.005	0.935 ± 0.004	0.942 ± 0.004	0.895 ± 0.004

Table 5. Atmospheric transmittance (τ_j), atmospheric path radiance ($L_{a,j}$), downwelling sky irradiance divided by π ($F_{\text{sky},j}/\pi$), and downwelling atmospheric radiance at nadir ($L_{d,j}(0^{\circ})$) for the ASTER TIR channels and the three days considered.

Date	Channel	τ_j	$L_{a,j}$ ($\text{Wm}^{-2}\text{sr}^{-1}\mu\text{m}^{-1}$)	$F_{\text{sky},j}/\pi$ ($\text{Wm}^{-2}\text{sr}^{-1}\mu\text{m}^{-1}$)	$L_{d,j}(0^{\circ})$ ($\text{Wm}^{-2}\text{sr}^{-1}\mu\text{m}^{-1}$)
August 3, 2004	10	0.570	3.044	4.897	3.813
	11	0.681	2.296	3.713	2.750
	12	0.750	1.830	2.955	2.054
	13	0.775	1.861	2.986	1.958
	14	0.745	2.076	3.258	2.200
August 12, 2004	10	0.573	3.068	4.769	3.697
	11	0.684	2.342	3.667	2.711
	12	0.752	1.888	2.967	2.056
	13	0.768	1.967	3.064	2.011
	14	0.738	2.201	3.353	2.266
July 21, 2005	10	0.577	3.188	4.637	3.600
	11	0.683	2.440	3.683	2.715
	12	0.746	2.012	3.093	2.139
	13	0.760	2.107	3.251	2.147
	14	0.730	2.332	3.503	2.380

Table 6. Comparison between simulated and ASTER calibrated at-sensor radiances ($Wm^{-2}sr^{-1}\mu m^{-1}$) for rice. The relative difference is $(L_{s,j}(\text{sim})-L_{s,j}(\text{c}))/L_{s,j}(\text{sim})$. T_g-T_j is the difference between the ground LST and the temperature calculated from $L_{s,j}(\text{c})$ and Eq. (12). The last column gives the emissivity from $L_{s,j}(\text{c})$ and Eq. (13).

Date	Channel	$L_{s,j}(\text{sim})$	$L_{s,j}(\text{c})$	Rel. Diff. (%)	T_g-T_j (°C)	ϵ_j
August 3, 2004	10	8.720	8.493	2.6	2.2	0.918
	11	9.238	9.070	1.8	1.3	0.956
	12	9.608	9.484	1.3	0.9	0.970
	13	9.733	9.695	0.4	0.3	0.985
	14	9.361	9.330	0.3	0.3	0.985
August 12, 2004	10	8.605	8.467	1.6	1.3	0.935
	11	9.116	8.947	1.9	1.4	0.945
	12	9.475	9.317	1.7	1.2	0.955
	13	9.581	9.586	-0.1	0.0	0.985
	14	9.260	9.245	0.2	0.1	0.981
July 21, 2005	10	8.723	8.463	3.0	2.5	0.909
	11	9.156	8.974	2.0	1.5	0.954
	12	9.487	9.360	1.3	1.0	0.971
	13	9.600	9.554	0.5	0.4	0.985
	14	9.284	9.184	1.1	1.0	0.972

Table 7. Difference between the ground measured LSTs (MOD28 SST for sea) and ASTER derived LSTs, in °C.

	GDAS		NRL	
	Rice	Sea	Rice	Sea
3-Aug-04	-1.1	-0.4	-0.9	-0.7
12-Aug-04	-0.8	-0.9	-1.9	-2.0
21-Jul-05	-0.2	-0.6	-2.0	-2.3

Table 8. Coefficients α_j ($Wm^{-2}sr^{-1}\mu m^{-1}/DN$) and β_j ($Wm^{-2}sr^{-1}\mu m^{-1}$) and determination coefficient r^2 for the adjustment of ASTER at sensor radiances (Eq. 14) for the ASTER TIR channels and the scenes indicated.

Date	Channel	α_j	β_j	r^2
August 3, 2004	10	0.012908	-5.982	0.9996
	11	0.010369	-3.682	0.9998
	12	0.009087	-2.687	0.9997
	13	0.007389	-2.451	1.0000
	14	0.007210	-3.057	0.9989
August 12, 2004	10	0.012796	-6.113	0.9994
	11	0.010419	-3.859	0.9997
	12	0.008995	-2.640	0.9994
	13	0.007430	-2.587	1.0000
	14	0.007320	-3.378	1.0000
July 21, 2005	10	0.013155	-6.639	0.9993
	11	0.010774	-4.480	1.0000
	12	0.009265	-3.131	0.9996
	13	0.007538	-2.831	1.0000
	14	0.007602	-3.908	0.9986